Light-Induced Charge Transfer in Two-Dimensional Hybrid Lead Halide Perovskites

Peer-reviewed author version

VAN LANDEGHEM, Melissa; VAN GOMPEL, Wouter; HERCKENS, Roald; LUTSEN, Laurence; VANDERZANDE, Dirk; VAN DOORSLAER, Sabine & Goovaerts, Etienne (2021) Light-Induced Charge Transfer in Two-Dimensional Hybrid Lead Halide Perovskites. In: Journal of physical chemistry. C, 125 (33) , p. 18317 -18327.

DOI: 10.1021/acs.jpcc.1c05005
Handle: http://hdl.handle.net/1942/35398

Light-Induced Charge Transfer in Two-Dimensional Hybrid Lead Halide Perovskites

Melissa Van Landeghem,[†] Wouter Van Gompel,[‡] Roald Herckens,[‡] Laurence Lutsen,[‡] Dirk Vanderzande,[‡] Sabine Van Doorslaer,[¶] and Etienne Goovaerts[*,†]

[†]*Department of Physics, University of Antwerp, Universiteitsplein 1, 2610 Antwerpen, Belgium*

[‡]*Hybrid Materials Design (HyMAD), Institute for Materials Research (IMO-IMOMEC), Hasselt University, Agoralaan 1, 3590 Diepenbeek, Belgium*

[¶]*Department of Chemistry, University of Antwerp, Universiteitsplein 1, 2610 Antwerpen, Belgium*

E-mail: etienne.goovaerts@uantwerpen.be

Abstract

2D hybrid perovskites consisting of layers of lead halide octahedra separated by long organic linker cations have great potential for functional material design towards tailored optical and electronic properties. Here, we report the first direct observation of light-induced charge transfer in a series of novel 2D perovskites incorporating conjugated linkers based on the carbazole molecule. Dedicated electron paramagnetic resonance (EPR) experiments and supporting quantum-chemical calculations reveal that excitons generated in the lead halide layer undergo charge transfer (CT) at the organic-inorganic interface resulting in a positive polaron delocalized over several carbazole moieties and a partner electron residing in the inorganic layer. The occurrence of such CT processes in these materials not only offers interesting new perspectives for the functionalization of future 2D perovskites, but could also lead to a better understanding of the unusual broadband emission reported for this material class, which has been directly related to polaronic effects.

Introduction

While 3D lead halide perovskites already demonstrated excellent performance in thin-film photovoltaics,[1] their 2D counterparts have recently emerged as highly promising materials due to their superior stability in solar-cell devices[2,3] and their tunable light-emitting properties.[4–7] Such 2D or Ruddlesden-Popper perovskites are composed of alternating layers of organic cations separated by a number (n) of perovskite sheets consisting of cornersharing lead halide octahedra. Often, a distinction is made between 2D layered ($n = 1$) and 2D multi-layered perovskites ($n > 1$). Because of the fewer structural constraints compared to their 3D equivalents, this material class allows for more complex organic molecules to be embedded in the perovskite framework and hence combines the outstanding opto-electronic properties of lead halide perovskites with the versatility of organic chemistry. The intrinsic layered structure moreover behaves as a series of quantum wells, wherein the electron and

hole wavefunctions are confined to the inorganic layer leading to large exciton binding energies of 150-400 meV.[8,9] The resulting electro-optical properties are therefore highly tunable through variation of the organic linker and the thickness of the perovskite layer.[10] Finally, due to the hydrophobic nature of these linker molecules, the organic layer acts as a natural barrier against moisture, thereby strongly enhancing the ambient stability of these materials compared to their 3D counterparts.[11–13]

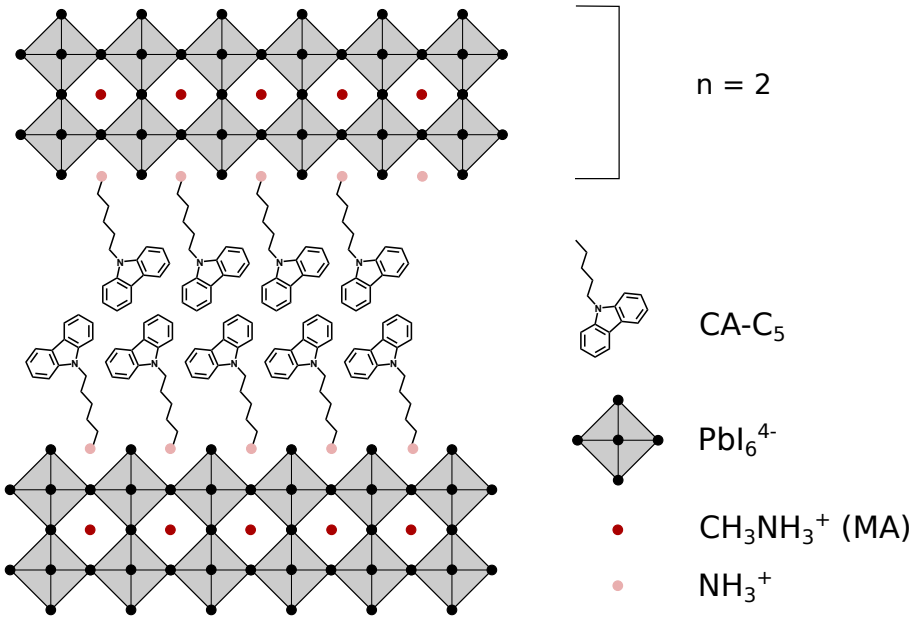

Figure 1: Schematic crystal structure of the $(CA{-}C_5H_{10}NH_3)_2MA_{n-1}Pb_nX_{3n+1}$ 2D hybrid perovskites (shown for $n = 2$).

The materials studied in this work are a series of PbI-based (multi-)layered perovskites with a carbazole (CA) derivative as organic linker (schematic crystal structure in Figure 1). The incorporation of chromophores with an extended conjugated π-system such as carbazole into 2D perovskites is of great interest for functional materials engineering. The first application of carbazole as an organic linker was reported by Era *et al.* in a fundamental study on single-layered PbBr perovskites.[14,15] Although these materials were not suited for solar cells, they exhibited an interesting increase of the in-plane conductivity compared to both polyvinylcarbazole and layered PbBr perovskites with insulating linkers. More recently, Pas-

sarelli *et al.* demonstrated that the use of such conjugated organic linkers can indeed improve the photovoltaic properties of 2D perovskites.[16] The incorporation of carbazole derivatives into a multi-layered perovskite framework was first established in a proof-of-principle study by part of the authors.[17] The higher-n perovskites were found to have charge diffusion lengths comparable to 3D methylammonium (MA) lead iodide and achieved PCEs of 7% in solar cells, comparable to reference devices based on phenethylammonium-linked perovskites, the literature standard for 2D perovskite solar cells (PeSCs). At the same time, the carbazole-linked perovskites exhibited a superior stability against moisture, both at the material and device level, an important advantage in any future opto-electronic application.

Quite surprisingly, many 2D hybrid perovskites are white-light emitters, with unusually broad ($\sim$ 100 nm) and highly Stokes-shifted ($\sim$ 1 eV) luminescence.[18,19] Similar broadband emission has also been observed in single-layered carbazole-linked perovskites.[17] Owing to the ionic character of the lattice and the importance of electron-phonon coupling in these materials, the formation of self-trapped states and polarons has often been put forward as a possible origin of this phenomenon. Several experimental observations support this hypothesis: (i) thermal activation of the broadband luminescence as observed in temperature-dependent PL studies,[8] which is consistent with the energetic barrier posed by the lattice deformation associated with the self-trapping; (ii) white-light emission occurring on the same timescale ($<$ 100 fs) as the Pb-halide bond vibrations as demonstrated by ultra-fast transient absorption and THz spectroscopy;[20] (iii) the absence of crystal-size effects on the emission properties which rules out surface states as the underlying radiative recombination centers;[18] (iv) the correlation between the efficiency of broadband emission in Br-based 2D perovskites with the degree of structural deformation in the lattice, more specifically the out-of-plane tilting of the lead-halide octahedra;[21] (v) the presence of fine structure in the emission spectra due to distinct excitonic transitions coupled to specific vibrational modes as revealed by impulsive stimulated Raman spectroscopy[22,23] and detailed analysis of exciton absorption spectra.[24,25] Yet, at present no experimental studies give any microscopic insight

into the nature and formation of these polaronic centers. Herein, a spin-sensitive technique such as electron paramagnetic resonance (EPR) has the unique potential to directly identify and characterize such polaronic states and has already been successfully applied for the study of polarons and self-trapped states in organic semiconductors[26] and more closely-related materials such as lead halides[27,28] and oxide perovskites.[29] In particular, the combination of dedicated hyperfine spectroscopy with quantum-mechanical computations of the EPR parameters offers detailed structural information on the direct surroundings of the polaron and hence gives invaluable insight into the delocalization and local symmetry of the trapping site.[26]

In this work, we use EPR to directly probe light-induced polarons in carbazole-linked PbI-based 2D perovskites with $\langle n \rangle = 1, 2, 10$. We report the observation of positive polarons in the organic layer, which is further supported by density functional theory (DFT) computations of the spectroscopic parameters. Since carbazole is transparent for the applied photo-excitation energies, we argue that the polarons are formed via interfacial charge transfer (CT) from excitons generated in the inorganic layer. While direct signatures of the partner electron in the inorganic layer could not be detected, the observation of CT in these materials nevertheless reveals a potentially important mechanism for the generation of emissive self-trapped states in the lead-halide layer. As such, these results shed a new light on our understanding of broadband emission in layered perovskites and moreover offers interesting perspectives for future functionalization towards unique synergistic properties of the organic and inorganic layer.

Methods

Sample preparation

$(CA{-}C_5H_{10}NH_3)_2MA_{n-1}Pb_nI_{3n+1}$ films ($\langle n \rangle = 1, 2, 10$) were cast from precursor solutions as described in.[17] Samples for X-band EPR were prepared from dropcasts on transparent polyethylene naphtalate (PEN) substrates, which resist the thermal annealing step required to form the 2D structure.[17] The samples were directly mounted into a quartz tube (I.D. 3 mm, O.D. 4 mm) by stacking multiple narrow strips cut from the dried film. W-band EPR samples were prepared by scratching off films deposited on glass substrates and subsequently transferring the collected material into a quartz sample tube (I.D. 0.6 mm, O.D. 0.84 mm).

Optical spectroscopy

Optical absorption spectra were measured on a Cary 5000 UV-Vis-NIR spectrophotometer from Agilent Technologies, a cleaned quartz substrate was used as calibration background.

EPR experiments

Pulsed X-band EPR experiments were recorded on a Bruker Elexsys E580 spectrometer (mw frequency: 9.75 GHz) equipped with a liquid helium cryostat (Oxford Instruments). To allow for light-induced experiments, the sample could be illuminated inside the cavity with the output of a continuous-wave (CW) 447 nm diode laser (CNI lasers, MDL-III-447-300mW) entering the sample tube via a fused silica optical fiber (core diameter: 100 μm, laser power at the end of the fiber: 20 mW). Electron spin echo (ESE)-detected EPR spectra were recorded using the $\pi/2 - \tau - \pi - \tau -$ echo sequence with $t_{\pi/2} = 16$ ns, $t_\pi = 32$ ns and interpulse delay $\tau = 162$ ns. The 2D three-pulse electron-spin-echo envelope modulation (ESEEM) experiment was performed using the pulse sequence $\pi/2 - \tau - \pi/2 - T - \pi/2 - \tau -$ echo, while incrementing the time intervals τ and T in steps of 16 ns from 108 ns to 412 ns, and from 84 ns to 4164 ns, respectively. In order to remove unwanted echoes, a four-step phase cycle

was applied. The ESEEM data were processed as follows. The time traces were baseline-corrected with a third-order polynomial, apodized with a Hamming window and zero-filled. After a two-dimensional Fourier transform, the absolute-value spectra were computed and summed along the τ-dimension to eliminate blind-spot effects. X-band electron-electron double resonance (ELDOR)-detected NMR (EDNMR) was performed using the standard sequence HTA $- t_d - \pi/2 - \tau - \pi - \tau -$ echo with the length of the high turning angle (HTA) pulse t_{HTA} optimized to 8 μs and t_d = 3 μs, $t_{\pi/2}$ = 12 ns and τ = 128 ns. All X-band experiments were performed at 15 K and with a shot repetition rate of 67 Hz.

W-band EPR experiments were performed on a Bruker Elexsys E680 W-band EPR spectrometer (mw frequency: 94.03 GHz), equipped with a standard single-mode cylindrical resonator from Bruker and a continuous-flow cryostat and superconducting magnet from Oxford Instruments. CW photo-excitation of the sample at 447 nm, 501.7 nm and 532 nm was achieved by illumination with a diode laser (CNI lasers, MDL-III-447-300mW), an Ar^+-laser (Spectraphysics 2020) and a frequency-doubled Nd:YAG laser (CNI lasers, MGL-III-532-300mW), respectively. Via a fused silica optical fiber (core diameter: 600 μm) the laser beam was directed into the quartz sample tube which acts as a light guide (20 mW laser power at the end of the fiber). All experiments were performed at 15 K and with a shot repetition rate of 67 Hz, unless stated otherwise. The ESE-detected EPR spectra were recorded using the pulse sequence $\pi/2 - \tau - \pi - \tau -$ echo with $t_{\pi/2}$ = 120 ns, t_π = 240 ns and interpulse delay τ = 360 ns. A two-step phase-cycle was applied to remove all unwanted echoes. All ESE-detected EPR spectra are presented as difference spectra (light-minus-dark) in order to determine the light-induced components. To allow for direct comparison, all of the presented field-swept spectra were rescaled to the same mw frequency (94.03 GHz) to account for small frequency differences between the experiments. W-band EDNMR was performed under continuous illumination using the HTA $- t_d - \pi/2 - \tau - \pi - \tau -$ echo pulse sequence with t_{HTA} = 24 μs, t_d = 4 μs and the same pulse lengths and delays for the detection sequence as in the ESE-detected EPR experiments.

Simulations of the EPR spectra were performed with EasySpin 5.1.3.[51]

DFT computations

Spin-unrestricted DFT calculations of the singly-charged oxidation states of the carbazole derivative were performed with the ORCA package (version 2.9.1).[52–54] In all calculations, the NH_3^+ group at the end of the alkyl chain was replaced by a CH_3 group. The first set of calculations involved an isolated CA$-C_6H_{13}$ molecule, later also a pair of stacked CA$-C_6H_{13}$ units was considered to better reproduce the close-packing expected within the perovskite host. For the isolated molecule, the structure geometry was first optimized using the BP86 functional[55] and the SVP basis set[56] for all atoms. The dimer calculation started from an antiparallel configuration of the carbazole groups with an initial distance between the backbones of both molecules of about 4 Å, similar to the intermolecular distance derived from XRD data on the related $(CA-C_5H_{10}NH_3)_2PbBr_4$ compound presented in.[15] Since convergence of the self-consistent field cycle could not be reached with a GGA-functional (BP86), we used the hybrid B3LYP functional[55,57] for the entire structural relaxation procedure which posed no further convergence problems. For both systems, single-point computations of the principal g-values were performed using the B3LYP functional combined with the EPR-II basis set.[58] All calculations were performed in vacuo.

Results

Formation, structure and optical properties

The $(CA-C_5H_{10}NH_3)_2MA_{n-1}Pb_nI_{3n+1}$ films were spin coated from CA$-C_5H_{10}NH_3I$, CH_3NH_3I and PbI_2 precursor solutions and post-annealed to obtain the desired 2D perovskite following the procedure of Herckens *et al.*[17] The synthesis of the CA$-C_5H_{10}NH_3I$ precursor is described in detail in the SI. The stoichiometric ratios of the precursors in the solution were determined with respect to a targeted value of n. Except for the single-layered perovskite with

$n = 1$ which is phase-pure, it is expected that the films also contain traces of perovskites with slightly smaller or larger n. This has been reported earlier for related multi-layered perovskites incorporating large organic cations.[30] In this work, the samples will therefore be denoted by their respective nominal $\langle n \rangle$ based on the precursors' stoichiometry, wherein the brackets indicate that these films could contain residues of perovskites with a different number of layers n. A more elaborate discussion on the n-distribution in these materials based on optical absorption data is included in the SI.

The 2D nature of the compounds was established in previous work by some of the authors.[17] Therein, X-ray diffraction (XRD) data on films revealed a series of reflections characteristic for 2D layered perovskites. For $\langle n \rangle = 1, 2$, the layers were found to be oriented parallel to the substrate, while for $\langle n \rangle \geq 3$ the preferential growth direction changes towards a perpendicular orientation of the 2D perovskite with respect to the substrate. Full

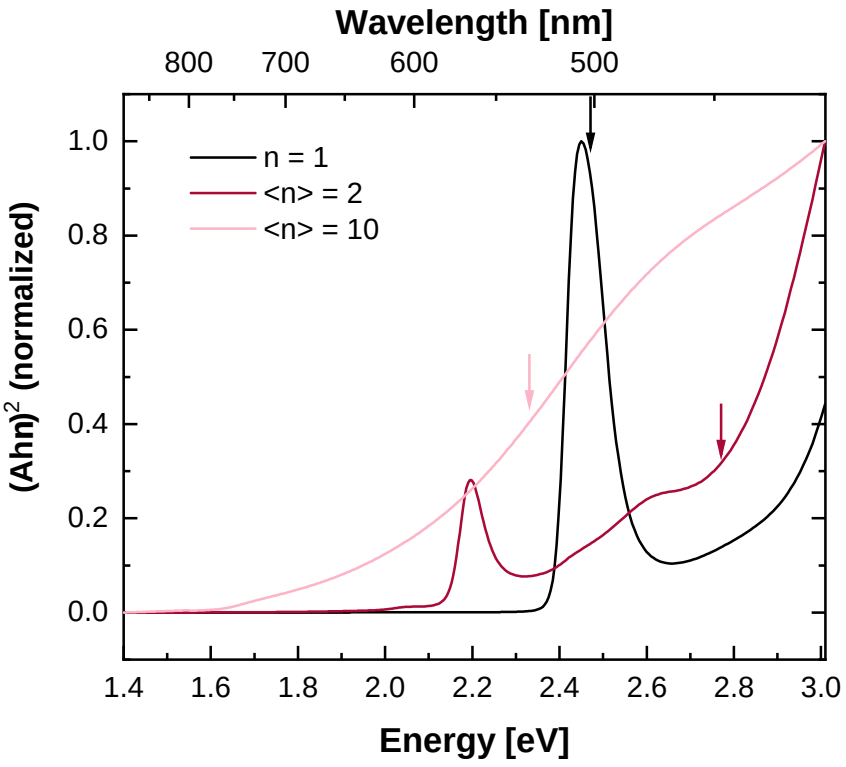

Figure 2: Normalized absorption spectra (Tauc plot) of the $(CA{-}C_5H_{10}NH_3)_2MA_{n-1}Pb_nI_{3n+1}$ films with different (targeted) $\langle n \rangle$. The arrows mark the different photo-excitation energies used in the LI-EPR experiments on the $\langle n \rangle = 1, 2, 10$ samples.

XRD analysis of the films studied in this work revealing the 2D nature of the perovskites is included in the SI. The reduced dimensionality of the perovskites is also apparent from the distinct excitonic peaks present in their absorption spectra as shown in Figure 2. The excitonic absorption shifts to lower energy for larger values of n, *i.e.* 2.45 eV for $n = 1$ and 2.19 eV for $n = 2$, correlating well with the reduced effect of quantum confinement when increasing the inorganic layer thickness (see Figure S8 for the determination of the optical gaps using the Tauc plot method). The absorption spectrum of the quasi-3D perovskite with $\langle n \rangle = 10$ features a band gap of about 1.6 eV, which is very close to the optical gap of 3D $MAPbI_3$. As mentioned earlier, these materials also feature the remarkable broadband emission characteristic for many 2D hybrid perovskites, which is most apparent for the low-n compounds (see SI).

Light-induced EPR

Because of the excitonic character of the absorption spectra, the photo-excitation energy had to be varied in the LI-EPR experiments for each of the samples with different $\langle n \rangle$. As such, the $n = 1$ sample was photo-excited at 501.7 nm (2.47 eV), very close to its excitonic absorption peak. The $\langle n \rangle = 2$ and $\langle n \rangle = 10$ sample were illuminated at 447 nm (2.77 eV), respectively, 532 nm (2.33 eV) which is well within their respective absorption bands. It is important to note that absorption by the carbazole molecules occurs in the UV at energies above 3.45 eV (359 nm) (see SI for the absorption spectrum of carbazole). This is significantly higher than any of the photo-excitation energies used. Hence, we can safely assume that in all samples the primary excitons are generated by light absorption within the inorganic octahedral layers and no light is absorbed by the organic spacer.

Figure 3 shows the X-band (9.75 GHz) and W-band (94.03 GHz) LI-EPR spectra of the 2D perovskites with $\langle n \rangle = 1, 2, 10$. No significant dark signal was observed in any of the samples (see SI). All of the 2D perovskites feature a similar EPR spectrum upon illumination, which was found to be partly reversible at 15 K with a reduction in signal intensity of

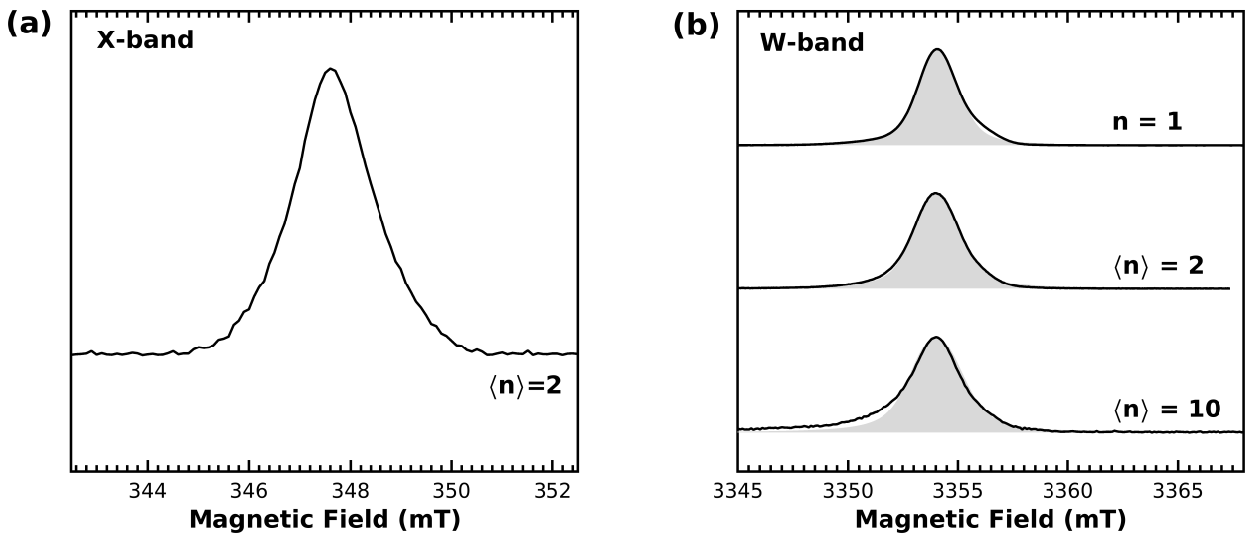

Figure 3: X-band (a) and W-band (b) light-induced ESE-detected EPR spectra of the 2D perovskites $(CA{-}C_5)_2MA_{n-1}Pb_nI_{3n+1}$ with $\langle n\rangle = 1, 2, 10$ recorded at 15 K. The $n = 1$ perovskite was photo-excited at 501.7 nm (2.47 eV), $\langle n\rangle = 2$ at 447 nm (2.77 eV) and $\langle n\rangle = 10$ at 532 nm (2.33 eV). The W-band spectra were brought to the same mw frequency and normalized to allow for easy comparison. Simulations of the EPR spectra are shown in grey. The principal g-values and linewidths used in the simulations are summarized in Table 1. For consistency with later simulations shown in this work, the simulations here also take into account the hyperfine couplings to two equivalent ^{14}N nuclei summarized in Table 2. The latter are unresolved in the ESE-detected spectra, but significantly affect the line broadening.

about 50% when the light is switched off. The EPR spectrum disappears completely after the samples have been heated to room temperature. Both the position of the line close to the free electron g-value, *i.e.* $g_e = 2.002319$, and its narrow width (∼8 mT in W-band) suggest that the signal stems from an organic radical center. In these materials, such an organic radical could be either centered on the MA group or the carbazole linker. Yet, the close similarity between the spectra of the $\langle n\rangle = 2, 10$ samples and that of the single-layered perovskite, which does not contain any MA cations, rules out MA radicals as possible origin for the LI-EPR signal. Hence, the spectra in Figure 3 are assigned to a singly-charged radical on the carbazole derivative. Taking into account that light absorption takes place only in the inorganic layer, this result indicates a reversible charging of the organic spacer layer via CT.

Despite the close similarity between the EPR spectra of the $\langle n \rangle = 1, 2, 10$ perovskites, small differences can be observed, in particular regarding their line shape. These deviations become most apparent when comparing the experimental traces with their respective simulations, shown in grey in Figure 3. The g-values corresponding to the best fit with the experimental data are summarized in Table 1. The experimental spectrum of each of the 2D perovskites can be simulated with a near-identical set of principal g-values, confirming the common nature of the EPR signal. Small differences in line shape between the $\langle n \rangle = 1, 2, 10$ perovskite spectra can be largely accounted for by adjusting the linewidth parameters in the simulation. Here, the line shape is fitted by an isotropic convolutional pseudo-voigtian broadening. This simple model is usually less approppriate as it doesn't account for the anisotropic sources of line broadening often present in EPR spectra and could be the reason for the small deviations observed in the tails of the spectra. Yet, the narrow overall width of the spectra complicates accurate fitting of the EPR line shape with more advanced inhomogeneous broadening mechanisms.

Table 1: Comparison of the experimental principal g-values of the radical on the carbazole linker molecules, and DFT-computed values for their cationic (monomer and dimer) and anionic (monomer only) radicals. The experimental g-values and linewidths ΔB were determined by simulation of the W-band EPR data shown in Figure 3. In the simulations an isotropic convolutional broadening with a pseudo-Voigtian lineshape was applied. The two tabulated broadening parameters correspond to the full width at half maximum of the corresponding Gaussian and Lorentzian profiles, respectively. The estimated error in the experimental g-values and linewidths is ± 0.0001 and ± 0.1 mT, respectively. For the g_z component of the $\langle n \rangle = 10$ perovskite a larger uncertainty of ± 0.0003 is assumed.

		g_x	g_y	g_z	ΔB (mT)
Exp	$\langle n \rangle = 1$	2.0025	2.0029	2.0034	(0.9,1.0)
	$\langle n \rangle = 2$	2.0024	2.0029	2.0034	(0.9,1.2)
	$\langle n \rangle = 10$	2.0024	2.0028	2.0036	(1.0,1.4)
DFT	CA$-C_6H_{13}^+$	2.0023	2.0030	2.0034	
	$(CA-C_6H_{13})_2^+$	2.0023	2.0030	2.0034	
	CA$-C_6H_{13}^-$	2.0023	2.0027	2.0029	

The assignment of the EPR spectra in Figure 3 to carbazole radicals can be further confirmed using hyperfine spectroscopy to probe couplings to magnetic nuclei surrounding the electron spin, in particular ^{14}N and ^{1}H. The presence of such couplings is a clear indication that the EPR signal stems from an organic center. To this end we have applied electron-electron double resonance (ELDOR)-detected NMR (EDNMR)[31,32] and electron-spin-echo envelope modulation (ESEEM).[33,34] Both are pulsed EPR techniques that rely on the interaction between the unpaired electron and surrounding nuclear spins to record an NMR-like spectrum revealing the nuclear frequencies of the system. Two regimes can be distinguished. In the weak coupling case ($|\nu_{\mathrm{I}}| > |A|/2$), the spectral response will be centered around the Larmor frequency ν_{I} of the nucleus and split by $|A|$, the strength of the hyperfine interaction. In the strong coupling case ($|A| > 2|\nu_{\mathrm{I}}|$), the spectrum will feature peaks centered about $|A|/2$ and split by $2\nu_{\mathrm{I}}$.[34] In powder-like solid-state samples such as the 2D perovskites studied here, the spectral analysis is further complicated by the fact that the hyperfine interaction is anisotropic and therefore characterized by a tensor rather than a scalar variable. As a result, the hyperfine spectra will strongly depend on the specific set of spins, corresponding to certain tensor orientations, detected by the pulse EPR experiment. This so-called 'orientational selection' can be carefully controlled by proper choice of the experimental settings and reveals the tensor character of the hyperfine interaction. Hence detailed analysis of these spectra allows to identify the coupled nuclei via their respective Larmor frequency and to quantify the strength of the corresponding hyperfine, and if present, nuclear quadrupole interactions, which would induce further smaller splittings.

The detection of hyperfine couplings to ^{14}N at W-band frequency was achieved using EDNMR. At typical W-band magnetic field strengths, the Larmor frequency of ^{14}N is about 10.3 MHz. The other relevant magnetic nuclei have their Larmor frequency in the 28-35 MHz range (^{207}Pb, ^{13}C and ^{127}I) or close to 142 MHz for ^{1}H. Except for ^{1}H, all of these nuclei would induce transitions within the sensitivity range of the EDNMR experiment. Yet, the recorded spectra featured no EDNMR response above 20 MHz (not shown), only

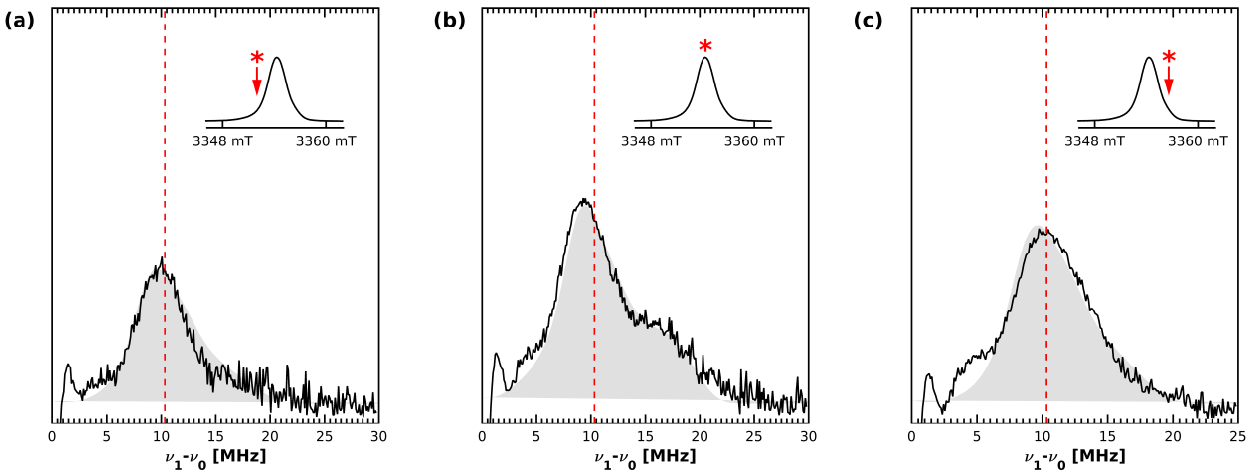

Figure 4: W-band EDNMR spectra of the $\langle n \rangle = 2$ perovskite recorded at 15 K for three different magnetic field positions: once at the low-field side (a), once at the maximum (b) and once at the high-field side (c) of the EPR spectrum, as indicated by a red asterisk in the corresponding EPR spectrum in the inset of each panel. The Lorentzian blindspot at $\Delta\nu = 0$ has been fitted and subtracted. The dashed red line indicates the Larmor frequency of ^{14}N at this magnetic field strength. The hyperfine parameters used for the simulations in grey are listed in Table 2. For consistency with later conclusions from supporting DFT computations, the simulations here consider two equivalent ^{14}N nuclei. The additional ^{14}N nucleus does not alter the spectrum qualitatively, but very slightly affects the line broadening.

low-frequency transitions stemming from hyperfine couplings to ^{14}N were observed.

Figure 4 presents the W-band EDNMR spectra of the $\langle n \rangle = 2$ perovskite recorded at three different magnetic field positions as indicated in the insets. Similar spectra were obtained for the $n = 1$ and $\langle n \rangle = 10$ samples (see SI). Clear qualitative differences can be observed between spectra recorded at different field positions, as a result of the rather narrow excitation bandwidth (~ 0.3 mT) of the soft detection pulses ($t_{\pi/2} = 120$ ns) and the sizeable **g** anisotropy. The fact that the EDNMR response depends strongly on this orientational selection is suggestive of a highly anisotropic hyperfine tensor. The EDNMR spectra in Figure 4a-c both feature a broad signal at about 10 MHz, which corresponds well with the weak coupling case to nitrogen nuclei centers. In the EDNMR spectra recorded at the maximum of the EPR spectrum (Figure 4b, S11b and S12b) an additional broad shoulder appears between 15 MHz and 20 MHz, which originates from strongly coupled rather than weakly coupled ^{14}N. The qualitative difference between the EDNMR spectra due to the

Table 2: Comparison of the experimental and DFT-computed ^{14}N hyperfine and quadrupole tensors of the radical on the carbazole linker. The experimental hyperfine couplings were obtained by simulating the W-band EDNMR spectra in Figure 4, S11 and S12. The Euler angles (α,β,γ) define the orientation of the tensor principal axes with respect to the g tensor frame. Herein γ is experimentally undetermined for the hyperfine and quadrupole tensors due to their (near-)axial symmetry.

		A_x[MHz]	A_y[MHz]	A_z[MHz]	α,β,γ [°]	e^2qQ[MHz]	η	α,β,γ [°]
Exp	$n = 1$	1	1	17	±55,90,-	-2.5	0.0	±5,90,-
	$\langle n \rangle = 2$	1	1	19	±55,90,-	-2.5	0.0	±20,90,-
	$\langle n \rangle = 10$	1	1	17	±55,90,-	-2.5	0.0	±10,90,-
DFT	CA−$C_6H_{13}^+$	2.30	2.18	56.10	2,90,0	-1.41	-0.18	5,90,0
	$(CA-C_6H_{13})_2^+$	1.21	1.14	31.81	11,90,-4	-2.65	-0.03	10,90,2
		0.85	0.80	25.43	-12,91,-2	-2.92	-0.03	-11,91,1
	CA−$C_6H_{13}^-$	-0.14	-0.14	1.02	3,90,0	-4.65	0.12	3,90,0

effect of orientational selection could be nicely reproduced in simulations (shown in grey in Figure 4, S11 and S12) assuming a ^{14}N nucleus with a highly anisotropic hyperfine tensor, with only one principal direction with strong coupling near to 20 MHz and very low values in the two other directions. The corresponding hyperfine parameters are summarized in Table 2. This result is a further confirmation that the LI-EPR signature does not originate from MA radical cations, which are known to exhibit a nearly isotropic coupling to ^{14}N of about 9-11 MHz.[35–37] Finally, we remark that the sharp features below 5 MHz, particularly in the spectra of the $\langle n \rangle = 10$ perovskite, are most likely not true signals but unknown experimental artefacts, as the linewidth of the peaks is much smaller than the expected resolution of the experiment (∼3 MHz). Moreover, EDNMR signals below 5 MHz can be considered unreliable due to the overlap with the central Lorentzian line and the possibility of inaccurate background subtraction. In addition, it is unclear which nuclei could give rise to these low-frequency transitions.

Hyperfine couplings to surrounding protons were further studied using X-band EDNMR and three-pulse ESEEM. Figure 5 shows the X-band EDNMR and ESEEM spectrum of

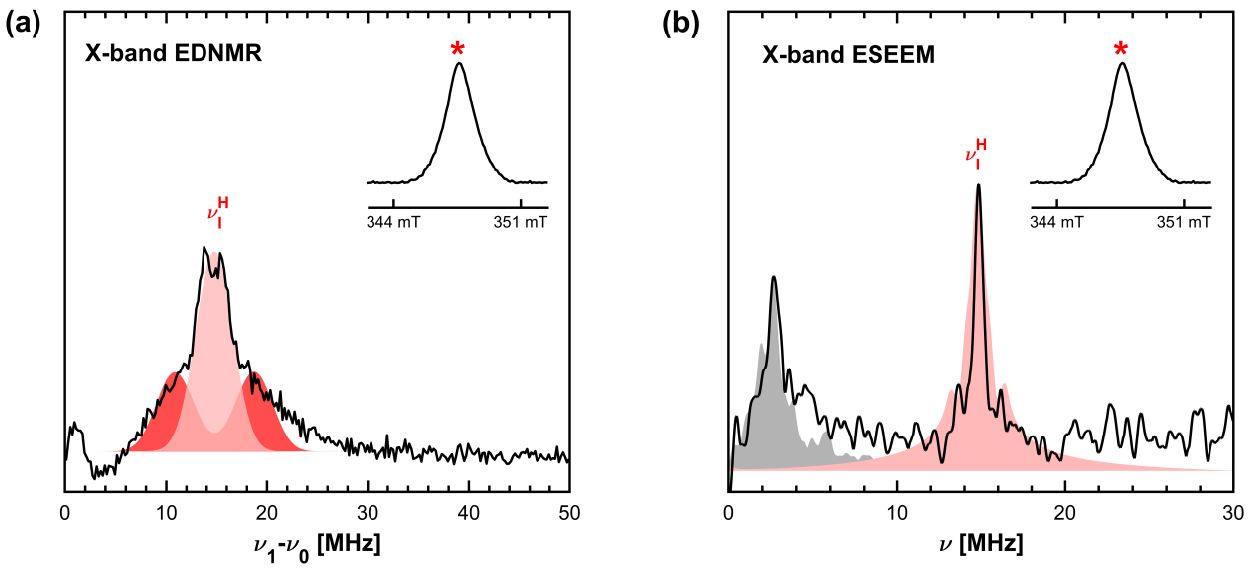

Figure 5: X-band EDNMR (a) and three-pulse ESEEM (b) of the $\langle n \rangle = 2$ perovskite recorded at $B = 347.7$ mT at a temperature of 15 K. The magnetic field position at which the EDNMR and ESEEM spectra were recorded is indicated by a red asterisk in the EPR spectrum in the inset. Black: experimental data. Colors: simulations based on the ^{14}N and ^{1}H DFT-computed hyperfine parameters for $(\mathrm{CA}{-}\mathrm{C_6H_{13}})_2^+$ summarized in Table 2, respectively, 3 (see section). Each of the simulations includes contributions from different groups of nuclei. Red: large ^{1}H couplings ($|A| > 10$ MHz) arising from protons of type $\mathrm{H^A}$, $\mathrm{H^C}$ and $\mathrm{H^E}$ (for the atom labelling see Figure 6). Pink: small ^{1}H couplings ($|A| < 3.5$ MHz) due to $\mathrm{H^B}$ and $\mathrm{H^D}$ protons along the carbazole backbone and a remote side-chain proton ($A_x, A_y, A_z = -0.3, -0.6, 0.7$ MHz). Grey: contribution of ^{14}N hyperfine and quadrupolar couplings.

the $\langle n \rangle = 2$ perovskite recorded at $B = 347.7$ mT ($g = 2.0031$), corresponding to the maximum of the EPR spectrum. Both spectra feature signatures of weakly coupled protons, evidenced by the presence of peaks centered about 14.8 MHz, the Larmor frequency of ^{1}H at X-band. In the EDNMR spectrum, the ^{1}H peak consists of an intense, sharp feature superimposed onto a broader structure of about 15-18 MHz wide. The maximal width of this signal provides an upper limit to the proton hyperfine couplings of the carbazole radical. In contrast, the ESEEM spectrum only features a very narrow peak at $\nu_{\mathrm{I}}^{\mathrm{H}}$ stemming from relatively small (< 2 MHz) ^{1}H couplings. The accidental suppression of larger hyperfine couplings in ESEEM spectra of multi-nuclear systems is a known effect, which unfortunately cannot be avoided experimentally.[38] Hence, we consider the broad wings of the ^{1}H peaks

in the EDNMR spectrum as sufficient proof for the presence of proton hyperfine couplings with $|A| \approx 15$ MHz. The ESEEM spectrum furthermore shows signals in the $0 - 6$ MHz range which originate from ^{14}N couplings. These low-frequency transitions are not resolved in the corresponding EDNMR experiment because they are masked by the central Lorentzian blindspot, which has been subtracted in the spectrum shown in Figure 5a.

DFT and comparison with experiment

In order to corroborate the assignment of the LI-EPR signal to a radical on the carbazole linker, we performed DFT calculations to underpin the magnetic resonance parameters obtained experimentally. Both (singly-charged) oxidation states of the carbazole derivative were considered, which would correspond to the final state of the molecule after either electron or hole transfer from excitons generated in the inorganic perovskite layer. As the oxidation state of such an organic radical is expected to affect the corresponding **g**-tensor, comparison of the theoretically predicted and experimental principal g values often allows identifying the charge state of the observed center.[39] In all calculations, the ammonium group at the end of the alkyl chain was replaced by a methyl group to avoid computational artefacts from maintaining the total charge at $+2$ instead of $+1$ for the positive radical.

The DFT-computed principal g values for the positive and negative radical on the carbazole derivative are summarized in Table 1 to allow for direct comparison with the experimental parameters from simulation of the spectra in Figure 3. For both oxidation states of the radical, the computed g values exhibit the same qualitative trends: one principal g value (g_x) very close to the free electron g; the other principal g values both larger than g_e. The DFT computations furthermore provide the orientation of the **g**-tensor principal axis system, which cannot be determined experimentally from the presented EPR powder spectra. As such, for both radicals, the same orientation of **g** with respect to the molecular axis system is obtained. The principal axis corresponding to g_x is found to be perpendicular to the molecular plane, in line with the small deviation from g_e.[40] Both g_y and g_z have their

principal axes lying in the molecular plane, respectively parallel and perpendicular to the symmetry axis of the carbazole backbone. An excellent agreement is found between the theoretically predicted g-values and the experimental parameters for the positive radical, which perfectly reproduces the experimental **g** anisotropy. For the negative radical, the agreement with experiment is slightly worse, in particular due to the underestimation of g_z. Yet, the deviation between the computed and experimental g values is still within the level of accuracy that can be expected from this type of calculations and the experimental determination via simulation. Hence, the oxidation state of the radical cannot be unambiguously assigned based on the comparison of the DFT-computed **g** tensors and the EPR data alone.

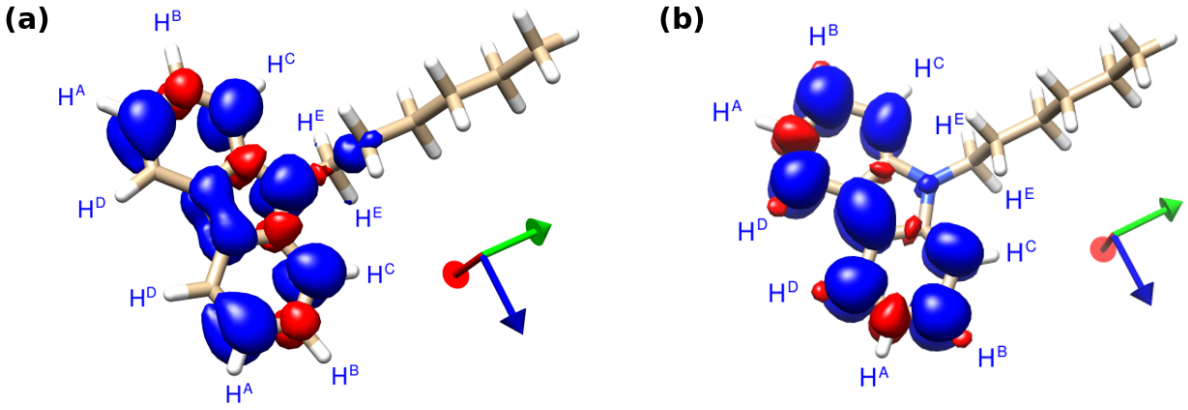

Figure 6: Spin density distribution of the positive (a) and negative (b) radical state of CA−C_6H_{13} based on DFT calculations. Red: Negative spin density. Blue: Positive spin density. Contour levels were fixed at -0.002 and 0.002, respectively. Principal axes **g**-tensor: x (red), y (green), z (blue).

While the **g**-tensor is a global probe of the electronic structure, the hyperfine parameters provide information on a single-atom level, allowing to probe the spatial distribution of the radicals over the molecular structure. A microscopic picture of the spatial extent of both CA−C_6H_{13} radicals is obtained by mapping out the DFT-computed spin density as illustrated in Figure 6. For both oxidation states, the radical is predicted to be delocalized over the entire conjugated backbone of the carbazole moiety, with very little spin density leaking out onto the alkyl side chain. The most striking difference between the positive and negative

radical is the amount of spin density localized on the nitrogen atom, which is reflected also in the corresponding DFT-computed ^{14}N hyperfine couplings summarized in Table 2. As expected, the much larger spin density on N calculated for CA$-$C$_6$H$_{13}^+$ leads to a very large component of the hyperfine tensor of 56 MHz. The coupling to ^{14}N is substantially weaker for the negative radical, given that the largest hyperfine value is only 1 MHz. Hence, while the theoretically predicted g-values did not allow to unambiguously assign the oxidation state of the observed radical, the ^{14}N hyperfine couplings in turn provide a clear fingerprint to distinguish between the positive and negative CA$-$C$_6$H$_{13}$ radical state. Looking back at the W-band EDNMR data in Figure 4, the experimental signatures of strongly coupled ^{14}N clearly indicate that the EPR response stems from positive radicals on the carbazole linker. The weak coupling predicted for the negative radical can never give rise to such spectral features.

Although the observed hyperfine anisotropy is qualitatively in line with the DFT calculation for CA$-$C$_6$H$_{13}^+$, the experimental maximum hyperfine component of about 19 MHz is overestimated by more than a factor of two (Table 2). This result suggests that the computed spin density is too strongly localized. It is important to consider that this first set of calculations involved a very crude model system, *i.e.* a single isolated CA$-$C$_6$H$_{13}$ molecule in vacuo. However, the individual carbazole derivatives confined within the layered perovskite host are expected to be closely stacked, which could lead to delocalization of radicals over multiple units and hence impact the corresponding magnetic resonance parameters. The enhanced π-π stacking of the carbazole-linkers due to a template effect of the inorganic layer has been described in earlier work on closely-related carbazole-linked PbBr perovskites by Era *et al.*[14,15] Hence, in order to assess the effect of this stacking on the radical delocalization and EPR parameters, we repeated our calculations for the positive radical for a close pair of carbazole units. To reflect the templating effect in the model geometry, the pair of carbazole linkers was forced into a similar relative orientation as observed in the experimental crystal structure of (CA$-$C$_5$H$_{10}$NH$_3$)$_2$PbBr$_4$.[15] In this initial configuration, the carbazole

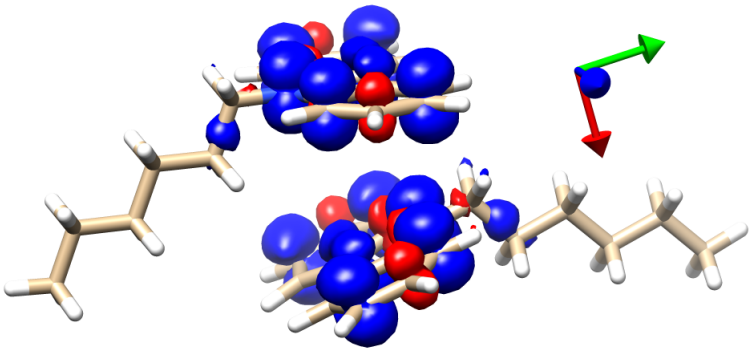

Figure 7: DFT-computed spin density distribution of the positive polaron on a closely-packed pair of CA−C_6H_{13} units. Red: Negative spin density. Blue: Positive spin density. Contour levels were fixed at -0.001 and 0.001, respectively. Principal axes **g**-tensor: x (red), y (green), z (blue).

backbones were antiparallel with the distance between the conjugation planes close to 4 Å. Before the EPR parameter calculations, a geometry optimization procedure was performed (without additional constraints), leading to a relaxed structure with similar intermolecular distance yet with the backbones of the two carbazole units slightly tilted with respect to the parallel starting configuration (see Figure 7). For compact notation, the calculations on the closely-packed pair of carbazole derivatives will be labeled $(CA{-}C_6H_{13})_2$.

For the composite system containing two carbazole derivatives, identical principal g values were obtained as for the isolated molecule (see Table 1). The corresponding spin density contour plot for the positive radical on the pair of carbazole units is shown in Figure 7. The spin density is found to be delocalized over the conjugated system of both molecules, indicating strong intermolecular π-π interactions in the organic linker layer. Due to the extended delocalization, the ^{14}N hyperfine couplings computed for the composite system are reduced by approximately a factor of two compared to the isolated molecule (Table 2). As a result, a good agreement is obtained between the experimental ^{14}N couplings and those predicted for the positive radical shared by two adjacent carbazole units. As such, it is likely more appropriate to abandon the picture of a localized organic radical and to describe the observed paramagnetic center as a small polaron that can be distributed over two or even

more neighbouring carbazole linkers.

While the strong anisotropy and near-axial symmetry of the computed hyperfine tensor is in good agreement with the EDNMR spectra in Figure 4, the orientation of its principal axes does not entirely agree with the experimental observations. Since the EDNMR spectra have been recorded at different magnetic field positions, the orientation of the hyperfine tensor frame with respect to the **g**-tensor axes can be inferred through careful analysis and simulation of these spectra. In particular, as the shoulder between 15 MHz and 20 MHz is directly associated with strongly coupled ^{14}N, the presence of this feature in Figure 4b and its (near) absence in Figure 4a-c immediately reveals that the hyperfine axis corresponding to the strong coupling component should be oriented more or less along the g_y axis. According to the best fit simulations, the unique axis of the axial ^{14}N hyperfine tensor indeed lies in the g_xg_y-plane, rotated 35° away from the g_y direction. Yet, the DFT computations of the isolated CA$-$C$_6$H$_{13}^+$ radical and the (CA$-$C$_6$H$_{13}$)$_2^+$ polaron both predict that the axis of the largest hyperfine coupling component would instead coincide almost exactly with the direction of g_x. A more elaborate discussion on the DFT-computed tensor frames and a possible explanation for this discrepancy between theory and experiment can be found in the supporting information.

In order to facilitate the interpretation of the X-band ESEEM and EDNMR spectra, also the proton hyperfine couplings were computed. Table 3 summarizes the ^{1}H hyperfine parameters calculated for the positive and negative radical on the carbazole linker and the (CA$-$C$_6$H$_{13}$)$_2^+$ polaron. Since the protons along the carbazole backbone are two-by-two equivalent, only one set of inequivalent protons is tabulated. The positive and negative radical feature clear qualitative differences in the calculated couplings of individual protons, as evidenced by the observation that the set of protons giving rise to the largest couplings is entirely complementary for the two oxidation states. Yet, the main observable that can be quantitatively compared with the experimental ESEEM and EDNMR data is the largest predicted ^{1}H couplings. As such, the positive and negative radical on an isolated carbazole

Table 3: DFT-computed ^{1}H hyperfine tensors of the positive and negative radical on the carbazole linker. Only the inequivalent protons are tabulated. The very small ^{1}H couplings (< 2 MHz) due to remote side-chain protons have been omitted. For the $(CA{-}C_6H_{13})_2^+$ model composed of two carbazole derivatives, a single representative set of protons is given. The hyperfine couplings due to the nearly-equivalent set of protons on the other carbazole unit are of similar magnitude. The labelling of the atoms is indicated in Figure 6.

		A_x[MHz]	A_y[MHz]	A_z[MHz]	α,β,γ [°]
$CA{-}C_6H_{13}^+$	H^A	-5.26	-22.07	-15.37	42,90,-2
	H^B	6.70	2.89	4.03	0,17,88
	H^C	-19.06	-5.68	-15.05	23,88,0
	H^D	-0.95	1.90	-2.15	39,90,-2
	H^E	20.53	13.26	14.80	3,24,-83
$(CA{-}C_6H_{13})_2^+$	H^A	-2.42	-7.77	-11.47	-2,52,78
	H^B	2.05	3.36	1.40	-29,77,-10
	H^C	-2.95	-7.83	-10.50	-2,20,-96
	H^D	-1.05	0.78	-1.51	30,76,-23
	H^E	11.81	8.08	8.65	-19,24,-91
$CA{-}C_6H_{13}^-$	H^A	3.89	2.14	6.59	0,43,86
	H^B	-25.45	-16.09	-7.04	0,15,87
	H^C	-10.19	-2.33	-6.89	18,89,-2
	H^D	-7.86	-16.66	-24.44	0,14,-93
	H^E	0.07	0.91	-1.00	-17,77,8

derivative are found to exhibit ^{1}H couplings up to 21 MHz, respectively, 25 MHz, too large compared to the upper limit of 15 MHz derived from the EDNMR linewidth. However, the spectral width of the ^{1}H contribution in the X-band EDNMR spectrum agrees nicely with the maximal couplings of about 12 MHz predicted for the positive polaron distributed over two carbazole units. Simulations based on the DFT-computed hyperfine parameters for the $(CA{-}C_6H_{13})_2^+$ polaron are included in Figure 5. In these simulations an empirical linewidth of 3.7 MHz was assumed. Clearly, the good agreement between the computed and experimental proton hyperfine couplings again confirms our earlier spectral assignment.

Discussion

The EPR spectra presented in this work revealed the partially reversible formation of a light-induced organic radical in each of the $n = 1, 2, 10$ layered perovskites. The combination of dedicated hyperfine spectroscopy with supporting DFT computations of the magnetic resonance parameters allowed to assign this LI-EPR signature to a positive polaron delocalized over the conjugated backbone of adjacent carbazole linkers within the organic layer. At the applied photo-excitation energies, no excitons can be generated directly inside the organic linker. Instead, the positive polaron could be formed via CT from excitons generated in the inorganic layer. A necessary condition for such a CT process to occur is a type-II band alignment of the different layers in the 2D perovskite. Figure 8 illustrates the proposed band alignment and hole-transfer mechanism in the carbazole-linked perovskites based on literature data for the relevant energy levels. A recent computational study of the closely-related $(CA{-}C_5H_{10}NH_3)_2PbBr_4$ perovskite demonstrated that the top of the valence band is due to states in the carbazole linker, while the bottom of the conduction band is composed of states in the inorganic layer, indeed confirming the type-II character of the interface.[15]

The assumption of an interfacial CT process implies the presence of a partner negative polaron residing in the inorganic layer. A number of LI-EPR experiments under different conditions have been performed to detect this partner electron, yet no relevant signatures could be observed. Such a negative polaron in the PbI_6 octahedral layer could be expected to bear great similarity to the self-trapped electron (STEL) in $PbCl_2$, which has been observed by X-band EPR by Nistor *et al.*[27] As such, we performed similar X-band CW EPR experiments on the $\langle n \rangle = 2$ perovskite with analoguous settings as reported in,[27] *i.e.* very high modulation amplitude (8 G, 15 G) and mw power (10 mW, 50 mW). The strong electron-phonon coupling enabling self-trapping in these materials also leads to fast spin-lattice relaxation times. As such, all experiments were performed at low temperature (4 K, 10 K, 60 K), in line with the observations in.[27] Finally, it should be noted that in $PbCl_2$ it was observed that the STEL centers were easily bleached out by illumination in the 470-670 nm range.

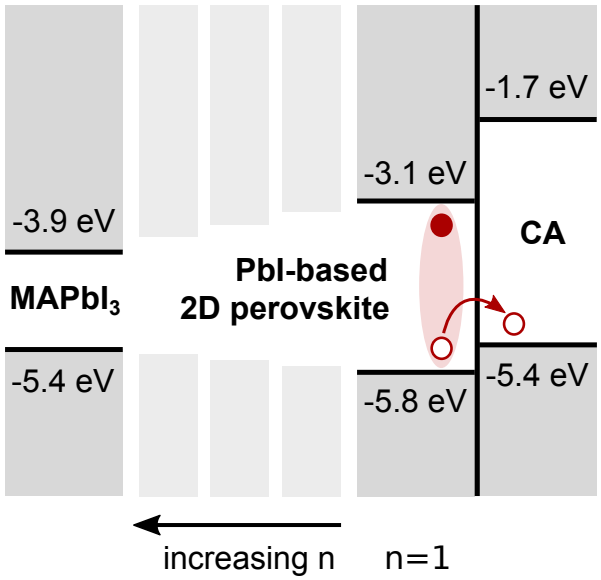

Figure 8: Suggestive banddiagram of the carbazole-linked perovskites illustrating the expected type-II band alignment and hole transfer mechanism. Frontier orbital energies of carbazole were taken from.[41] Band extrema for 3D $MAPbI_3$ and single-layered PbI-based perovskites from[42] and,[43] respectively.

This optical bleaching effect was put forward by Nistor *et al.* as one of the major factors inhibiting the detection of STEL centers by EPR in earlier studies. As such, special care was taken with respect to the photo-excitation conditions during our LI-EPR experiments dedicated to probing STEL-type centers. Several different approaches have been tested using low-power ($5 - 10\text{mW/cm}^2$) 447 nm laser light as photo-excitation source: (1) continuous illumination at low temperature during the EPR experiment; (2) short-term illumination for several minutes at 60 or 100 K followed by a freeze quench to 10 K and EPR detection in the dark; (3) illumination at 10 K followed by EPR detection in the dark. None of the described experiments featured any EPR signals besides the spectrum of the organic radical on the carbazole linker. Yet, it has to be stressed that electron-trapped centers on heavy-metal ions such as lead have often been hard to probe by EPR. In particular, the trapping at Pb^{2+} impurity sites in ionic crystals of electrons occupying the $6p^1$ orbital was in several studies convincingly evidenced by optical spectroscopy, but EPR observation could not be achieved and only related centers with additional perturbing defects such as charge compensating

vacancies and interstitials could be detected.[44–48] Hence, the absence of EPR signatures of the partner electron in the inorganic layer does not necessarily exclude its presence in the carbazole-linked perovskites. Possible explanations include: (i) ultrafast spin relaxation due to the presence of heavy atoms which could broaden the signal beyond detection; (ii) a rapid conversion of the negative polarons, for instance by efficient coupling between anion centers leading to an EPR silent ground state such as a (diamagnetic) singlet or a triplet with very large zero-field splitting. Nevertheless, the direct detection of such STEL centers in layered perovskites remains subject for further studies, in particular since the intriguing broadband emission observed in these materials has been suggested to be primarily governed by states trapped within the inorganic layer.[18,19,49]

Recently, Gélvez-Rueda *et al.*[50] reported the observation of a CT mechanism in layered perovskites incorporating an organic charge-transfer complex (CTC) composed of a pyrene donor and a tetracyanoquinodimethane acceptor. In contrast to the results presented in this work, the primary excitation in the latter system occurs in the CTC, followed by hole transfer to the lead halide layer. The resulting long-lived mobile charges in the inorganic layer were detected *via* transient absorption and microwave conductivity experiments. While qualitatively different, the results reported in[50] and in this work both indicate that charge separation via interfacial CT could present a new paradigm for the design and synthesis of novel 2D perovskites with unique properties. In particular, efficient CT from the tightly bound excitons generated in the inorganic layer could be leveraged to facilitate charge separation in these materials. Conversely, CT from excitons generated in the organic layer could potentially be exploited to increase the external quantum efficiency (EQE) of devices incorporating layered perovskites, if the absorption properties of the functionalized linker can be tuned to complement absorption by the inorganic layer.

Conclusion

In this work we have presented direct experimental evidence for the light-induced formation of positive polarons in the organic interlayer of PbI-based 2D perovskites with carbazole-linked ammonium molecules as spacer cations. The applied joint EPR-DFT approach allowed to unambiguously identify the charge state of the observed center and to map out the spatial delocalization of the polaron over multiple adjacent carbazole units in the organic layer. Because the applied photo-excitation energies were well below the absorption onset of the carbazole linkers, the polarons are assumed to be formed via hole transfer at the organic-inorganic interface from excitons generated in the PbI octahedral layer. Yet, so far no signature of the partner electron in the inorganic layer could be observed. To the best of our knowledge, this work represents the first direct observation of small polarons in hybrid layered perovskites. The light-induced CT mechanism as reported here is considered to be highly promising for the functionalization of novel 2D perovskites with unique synergistic properties of the organic and inorganic layer. Moreover, the further study of CT processes in layered lead halide perovskites may also contribute to the understanding of the broadband emission observed in these materials.

Acknowledgement

The authors want to acknowledge the Research Foundation Flanders (FWO – Vlaanderen) for support of this work through the PhD fellowship of M.V.L. (grant number 1185019N), the SB PhD fellowship of W.V.G. (project number 1S17516N), the funding of the SBO project called PROCEED (S002019N), the senior research project with grant number G043320N, and the M-ERA.NET project called PROMISES. Interreg Vlaanderen-Nederland is acknowledged for the funding of the PVopMAAT project.

Supporting Information Available

The following files are available free of charge.

- Figure S1: ^{1}H NMR of the CA$-$C$_5$ ammonium iodide salt
- Figure S2-S6: materials characterization by XRD
- Figure S7: absorption spectrum CA$-$C$_5$
- Figure S8 and Table S1-S2: optical band gaps from absorption data
- Figure S9 and Table S3-S4: excitonic emission peak energies from PL spectroscopy
- Figure S10: light and dark W-band EPR spectra
- Figure S11-S12: W-band EDNMR spectra $\langle n \rangle = 1$, 10 perovskites
- Figure S13: Orientation DFT-computed ^{14}N hyperfine tensors

Present address MVL: Institute for Materials Research (IMO-IMOMEC), Hasselt University, Agoralaan 1, 3590 Diepenbeek, Belgium

References

(1) Snaith, H. J. Perovskites: The Emergence of a New Era for Low-Cost, High-Efficiency Solar Cells. *J. Phys. Chem. Lett.* **2013**, *4*, 3623–3630.

(2) Tsai, H.; Nie, W.; Blancon, J.-C.; Stoumpos, C. C.; Asadpour, R.; Harutyunyan, B.; Neukirch, A. J.; Verduzco, R.; Crochet, J. J.; Tretiak, S. et al. High-efficiency two-dimensional Ruddlesden–Popper perovskite solar cells. *Nature* **2016**, *536*, 312–316.

(3) Grancini, G.; Roldán-Carmona, C.; Zimmermann, I.; Mosconi, E.; Lee, X.; Martineau, D.; Narbey, S.; Oswald, F.; De Angelis, F.; Graetzel, M. et al. One-Year stable perovskite solar cells by 2D/3D interface engineering. *Nat. Commun.* **2017**, *8*, 1–8.

(4) Saidaminov, M. I.; Mohammed, O. F.; Bakr, O. M. Low-dimensional-networked metal halide perovskites: The next big thing. *ACS Energy Lett.* **2017**, *2*, 889–896.

(5) Etgar, L. The merit of perovskite's dimensionality; can this replace the 3D halide perovskite? *Energy Environ. Sci.* **2018**, *11*, 234–242.

(6) Tsai, H.; Nie, W.; Blancon, J.-C.; Stoumpos, C. C.; Soe, C. M. M.; Yoo, J.; Crochet, J.; Tretiak, S.; Even, J.; Sadhanala, A. et al. Stable Light-Emitting Diodes Using Phase-Pure Ruddlesden-Popper Layered Perovskites. *Adv. Mater.* **2018**, *30*, 1704217.

(7) Lei, L.; Seyitliyev, D.; Stuard, S.; Mendes, J.; Dong, Q.; Fu, X.; Chen, Y. A.; He, S.; Yi, X.; Zhu, L. et al. Efficient Energy Funneling in Quasi-2D Perovskites: From Light Emission to Lasing. *Adv. Mater.* **2020**, *32*, 1906571.

(8) Cortecchia, D.; Yin, J.; Bruno, A.; Lo, S.-Z. A.; Gurzadyan, G. G.; Mhaisalkar, S.; Brédas, J.-L.; Soci, C. Polaron self-localization in white-light emitting hybrid perovskites. *J. Mater. Chem. C* **2017**, *5*, 2771–2780.

(9) Blancon, J.-C.; Stier, A. V.; Tsai, H.; Nie, W.; Stoumpos, C. C.; Traoré, B.; Pedesseau, L.; Kepenekian, M.; Katsutani, F.; Noe, G. T. et al. Scaling law for excitons in 2D perovskite quantum wells. *Nat. Commun.* **2018**, *9*, 2254.

(10) Saparov, B.; Mitzi, D. B. Organic–Inorganic Perovskites: Structural Versatility for Functional Materials Design. *Chem. Rev.* **2016**, *116*, 4558–4596.

(11) Smith, I. C.; Hoke, E. T.; Solis-Ibarra, D.; McGehee, M. D.; Karunadasa, H. I. A Layered Hybrid Perovskite Solar-Cell Absorber with Enhanced Moisture Stability. *Angew. Chemie Int. Ed.* **2014**, *53*, 11232–11235.

(12) Zheng, H.; Liu, G.; Zhu, L.; Ye, J.; Zhang, X.; Alsaedi, A.; Hayat, T.; Pan, X.; Dai, S. The Effect of Hydrophobicity of Ammonium Salts on Stability of Quasi-2D Perovskite Materials in Moist Condition. *Adv. Energy Mater.* **2018**, *8*, 1800051.

(13) Lee, D. S.; Yun, J. S.; Kim, J.; Soufiani, A. M.; Chen, S.; Cho, Y.; Deng, X.; Seidel, J.; Lim, S.; Huang, S. et al. Passivation of Grain Boundaries by Phenethylammonium in Formamidinium-Methylammonium Lead Halide Perovskite Solar Cells. *ACS Energy Lett.* **2018**, *3*, 647–654.

(14) Era, M.; Kobayashi, T.; Sakaguchi, K.; Tsukamoto, E.; Oishi, Y. Electric conduction of PbBr-based layered perovskite organic-inorganic superlattice having carbazole chromophore-linked ammonium molecule as an organic layer. *Org. Electron.* **2013**, *14*, 1313–1317.

(15) Era, M.; Yasuda, T.; Mori, K.; Tomotsu, N.; Kawano, N.; Koshimizu, M.; Asai, K. PbBr-Based Layered Perovskite Organic–Inorganic Superlattice Having Carbazole Chromophore; Hole-Mobility and Quantum Mechanical Calculation. *J. Nanosci. Nanotechnol.* **2016**, *16*, 3159–3167.

(16) Passarelli, J. V.; Fairfield, D. J.; Sather, N. A.; Hendricks, M. P.; Sai, H.; Stern, C. L.; Stupp, S. I. Enhanced Out-of-Plane Conductivity and Photovoltaic Performance in n = 1 Layered Perovskites through Organic Cation Design. *J. Am. Chem. Soc.* **2018**, *140*, 7313–7323.

(17) Herckens, R.; Van Gompel, W. T.; Song, W.; Gélvez-Rueda, M. C.; Maufort, A.; Ruttens, B.; D'Haen, J.; Grozema, F. C.; Aernouts, T.; Lutsen, L. et al. Multi-layered hybrid perovskites templated with carbazole derivatives: Optical properties, enhanced moisture stability and solar cell characteristics. *J. Mater. Chem. A* **2018**, *6*, 22899–22908.

(18) Dohner, E. R.; Jaffe, A.; Bradshaw, L. R.; Karunadasa, H. I. Intrinsic White-Light Emission from Layered Hybrid Perovskites. *J. Am. Chem. Soc.* **2014**, *136*, 13154–13157.

(19) Cortecchia, D.; Yin, J.; Petrozza, A.; Soci, C. White light emission in low-dimensional perovskites. *J. Mater. Chem. C* **2019**, *7*, 4956–4969.

(20) Park, M.; Neukirch, A. J.; Reyes-Lillo, S. E.; Lai, M.; Ellis, S. R.; Dietze, D.; Neaton, J. B.; Yang, P.; Tretiak, S.; Mathies, R. A. Excited-state vibrational dynamics toward the polaron in methylammonium lead iodide perovskite. *Nat. Commun.* **2018**, *9*, 1–9.

(21) Smith, M. D.; Jaffe, A.; Dohner, E. R.; Lindenberg, A. M.; Karunadasa, H. I. Structural origins of broadband emission from layered Pb–Br hybrid perovskites. *Chem. Sci.* **2017**, *8*, 4497–4504.

(22) Thouin, F.; Valverde-Chávez, D. A.; Quarti, C.; Cortecchia, D.; Bargigia, I.; Beljonne, D.; Petrozza, A.; Silva, C.; Srimath Kandada, A. R. Phonon coherences reveal the polaronic character of excitons in two-dimensional lead halide perovskites. *Nat. Mater.* **2019**, *18*, 349–356.

(23) Srimath Kandada, A. R.; Silva, C. Exciton Polarons in Two-Dimensional Hybrid Metal-Halide Perovskites. *J. Phys. Chem. Lett.* **2020**, *11*, 3173–3184.

(24) Straus, D. B.; Hurtado Parra, S.; Iotov, N.; Gebhardt, J.; Rappe, A. M.; Subotnik, J. E.; Kikkawa, J. M.; Kagan, C. R. Direct Observation of Electron–Phonon Coupling and Slow Vibrational Relaxation in Organic–Inorganic Hybrid Perovskites. *J. Am. Chem. Soc.* **2016**, *138*, 13798–13801.

(25) Neutzner, S.; Thouin, F.; Cortecchia, D.; Petrozza, A.; Silva, C.; Srimath Kandada, A. R. Exciton-polaron spectral structures in two-dimensional hybrid lead-halide perovskites. *Phys. Rev. Mater.* **2018**, *2*, 064605.

(26) Niklas, J.; Poluektov, O. G. Charge Transfer Processes in OPV Materials as Revealed by EPR Spectroscopy. *Adv. Energy Mater.* **2017**, *7*, 1602226.

(27) Nistor, S. V.; Goovaerts, E.; Schoemaker, D. Direct observation of electron self-trapping in PbCl2 crystals. *Phys. Rev. B* **1993**, *48*, 9575–9580.

(28) Iwanaga, M.; Azuma, J.; Shirai, M.; Tanaka, K.; Hayashi, T. Self-trapped electrons and holes in PbBr2 crystals. *Phys. Rev. B* **2002**, *65*, 2143061–2143068.

(29) Schirmer, O. F. *Defects and Surface-Induced Effects in Advanced Perovskites*; Springer Netherlands: Dordrecht, 2000; pp 75–88.

(30) Liu, J.; Leng, J.; Wu, K.; Zhang, J.; Jin, S. Observation of Internal Photoinduced Electron and Hole Separation in Hybrid Two-Dimentional Perovskite Films. *J. Am. Chem. Soc.* **2017**, *139*, 1432–1435.

(31) Schosseler, P.; Wacker, T.; Schweiger, A. Pulsed ELDOR detected NMR. *Chem. Phys. Lett.* **1994**, *224*, 319–324.

(32) Goldfarb, D. Eldor-detected NMR. *eMagRes* **2017**, *6*, 101–104.

(33) Rowan, L. G.; Hahn, E. L.; Mims, W. B. Electron-Spin-Echo Envelope Modulation. *Phys. Rev.* **1965**, *137*, 61.

(34) Schweiger, A.; Jeschke, G. *Principles of Pulse Electron Paramagnetic Resonance*; Oxford University Press: Oxford, U.K., 2001.

(35) Anderson, N. H.; Norman, R. O. C. Electron spin resonance studies. Part XXIX. Alkylamino and α-amino-alkyl radicals. *J. Chem. Soc. B* **1971**, 993–1003.

(36) Lyons, A. R.; Neilson, G. W.; Symons, M. C. R. Unstable intermediates. Part 113.—E.S.R. data for R 2 ĊXR 3 radicals, when X is from group IV or V. Evidence against significant d(π)—p(π) bonding. *J. Chem. Soc., Faraday Trans. 2* **1972**, *68*, 807–813.

(37) Poupko, R.; Rosenthal, I.; Elad, D. Photochemical decarboxylation of amino acids in the presence of metal ions. *Photochem. Photobiol.* **1973**, *17*, 395–402.

(38) Stoll, S.; Calle, C.; Mitrikas, G.; Schweiger, A. Peak suppression in ESEEM spectra of multinuclear spin systems. *J. Magn. Reson.* **2005**, *177*, 93–101.

(39) Ling, Y.; Van Mierloo, S.; Schnegg, A.; Fehr, M.; Adriaensens, P.; Lutsen, L.; Vanderzande, D.; Maes, W.; Goovaerts, E.; Van Doorslaer, S. Electronic structure of positive and negative polarons in functionalized dithienylthiazolo[5,4-d]thiazoles: A combined EPR and DFT study. *Phys. Chem. Chem. Phys.* **2014**, *16*, 10032–10040.

(40) Gast, P.; Groenen, E. J. J. EPR Interactions – g-Anisotropy. *eMagRes* **2016**, *5*, 1435–1444.

(41) Woon, K. L.; Nadiah, Z. N.; Hasan, Z. A.; Ariffin, A.; Chen, S.-A. Tuning the singlet-triplet energy splitting by fluorination at 3,6 positions of the 1,4-biscarbazoylbenzene. *Dyes Pigm.* **2016**, *132*, 1–6.

(42) Kim, H.-S.; Lee, C.-R.; Im, J.-H.; Lee, K.-B.; Moehl, T.; Marchioro, A.; Moon, S.-J.; Humphry-Baker, R.; Yum, J.-H.; Moser, J. E. et al. Lead Iodide Perovskite Sensitized All-Solid-State Submicron Thin Film Mesoscopic Solar Cell with Efficiency Exceeding 9%. *Sci. Rep.* **2012**, *2*, 591.

(43) Silver, S.; Yin, J.; Li, H.; Brédas, J.-L.; Kahn, A. Characterization of the Valence and Conduction Band Levels of n = 1 2D Perovskites: A Combined Experimental and Theoretical Investigation. *Adv. Energy Mater.* **2018**, *8*, 1703468.

(44) Stott, J. P.; Crawford Jr., J. H. Effect of Ionizing Radiation of Impurity-Vacancy Dipoles in Lead-Doped NaCl and KCl. *Phys. Rev. B* **1971**, *4*, 639.

(45) Nagli, L. E.; Dyachenko, S. V. Influence of a Vc- Vacancy on Luminescence of Pb+ Centres in Alkali Halides. *Phys. Stat. Sol. B* **1988**, *146*, 295.

(46) Goovaerts, E.; Nistor, S. V.; Schoemaker, D. Electron-spin resonance of a complex Pb+(6p1) defect in alkali halides. *Phys. Rev. B* **1983**, *28*, 3712.

(47) Heynderickx, I.; Goovaerts, E.; Nistor, S. V.; Schoemaker, D. Electron-Spin-Resonance Study of Pb+(1) Centers of the Laser-Active Structure in KCl and RbCl2). *Phys. Status Solidi* **1986**, *136*, 69–83.

(48) Goovaerts, E.; Nistor, S. V.; Schoemaker, D. Identification by ESR of Pb^{+}-type centres in lead-doped $SrCl_2$. *J. Phys. Condens. Matter* **1992**, *4*, 9259–9268.

(49) Yin, J.; Li, H.; Cortecchia, D.; Soci, C.; Brédas, J.-L. Excitonic and Polaronic Properties of 2D Hybrid Organic–Inorganic Perovskites. *ACS Energy Lett.* **2017**, *2*, 417–423.

(50) Gélvez-Rueda, M. C.; Van Gompel, W. T. M.; Herckens, R.; Lutsen, L.; Vanderzande, D.; Grozema, F. C. Inducing Charge Separation in Solid-State Two-Dimensional Hybrid Perovskites through the Incorporation of Organic Charge-Transfer Complexes. *J. Phys. Chem. Lett.* **2020**, *11*, 824–830.

(51) Stoll, S.; Schweiger, A. EasySpin, a comprehensive software package for spectral simulation and analysis in EPR. *J. Magn. Reson.* **2006**, *178*, 42–55.

(52) Neese, F. The ORCA program system. *Wiley Interdiscip. Rev. Comput. Mol. Sci.* **2012**, *2*, 73–78.

(53) Neese, F. Prediction of electron paramagnetic resonance g values using coupled perturbed Hartree-Fock and Kohn-Sham theory. *J. Chem. Phys.* **2001**, *115*, 11080–11096.

(54) Neese, F. Efficient and accurate approximations to the molecular spin-orbit coupling operator and their use in molecular g-tensor calculations. *J. Chem. Phys.* **2005**, *122*, 034107.

(55) Becke, A. D. Density-functional exchange-energy approximation with correct asymptotic behavior. *Phys. Rev. A* **1988**, *38*, 3098–3100.

(56) Schäfer, A.; Horn, H.; Ahlrichs, R. Fully Optimized Contracted Gaussian-Basis Sets for Atoms Li to Kr. *J. Chem. Phys.* **1992**, *97*, 2571–2577.

(57) Lee, C.; Yang, W.; Parr, R. G. Development of the Colle-Salvetti correlation-energy formula into a functional of the electron density. *Phys. Rev. B* **1988**, *37*, 785–789.

(58) Barone, V. In *Recent Advances in Density Functional Methods*; Chong, D. P., Ed.; World Scientific: Singapore, 1995; Vol. 1, pp 287–334.

Graphical TOC Entry